Inorganic Chemistry

Article

pubs.acs.org/IC

One-Step Bulk Synthesis of Stable, Near Unit-Cell Sized Oxide Nanoparticles and Nanoparticle Blends Using KO_2

Thomas E. Sutto*

Material Science and Technology Division, Code 6364, Naval Research Laboratory, 4555 Overlook Avenue SW, Washington, D.C. 20375, United States

Ⓢ *Supporting Information*

ABSTRACT: Presented here is a novel one-step synthesis of oxide or hydroxide nanoparticles using, for the first time, potassium superoxide (KO_2). This work demonstrates that the reaction of KO_2 with different salt solutions produces grams of stable, near unit-cell sized nanoparticles. This new synthetic technique is applied to representative elements from across the periodic table to rapidly produce nanometer sized oxides or hydroxides of Mg, Al, Y, Ti, Mn, Fe, Co, Ni, Cu, Zn, Sn, Tl, Pb, and Ce. This technique is also used to produce blends of nanoparticles, demonstrating the ability to prepare complex materials such as nanoparticulate blends of a lithium cathode material ($LiCoO_2$), the multiferroic compound ($BiMnO_{3+\delta}$), and the superconducting $YBa_2Cu_3O7_{-\gamma}$.

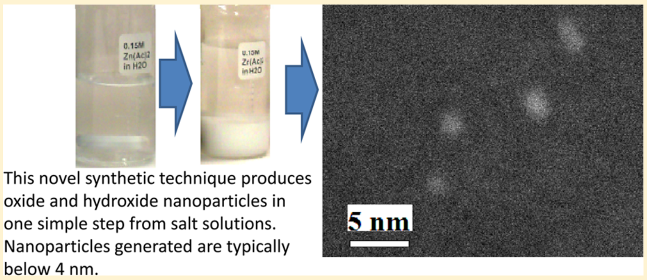

This novel synthetic technique produces oxide and hydroxide nanoparticles in one simple step from salt solutions. Nanoparticles generated are typically below 4 nm.

1. INTRODUCTION

First considered theoretically in the mid 1980s, nanometer-sized oxide particles were first synthesized several years later.[1,2] One of the first uses for metal oxide nanoparticles was Fe_2O_3 nanoparticles (≈50 nm), which were used for magnetic data storage.[2] Since that time, oxide nanoparticles have been shown to be crucial components in numerous applications: electronic and magnetic devices, energy storage and generation, and medical applications such as magnetic nanoparticles used for magnetic resonance imaging (MRI).[3−6] One example application of oxide nanoparticles is the Gretzel Solar cells, which use dye-coated TiO_2 nanoparticles to absorb incident radiation.[7] Metal oxide nanoparticles are also being explored as high-energy electrode materials for lithium batteries and Zn batteries.[8,9] In both of these cases, and in many other applications, particle size is critical to the utility of oxide nanoparticles. Decreased particle size results in increased surface area, which can significantly improve the performance of the oxide nanoparticle.[10,11]

Previously, the general approach toward preparing metal oxide nanoparticles involved the slow reaction of a weak oxidizing agent, such as hydrogen peroxide, with dilute solutions of metal salts or complexes in both aqueous and nonaqueous solvent systems. The metal concentrations, usually in the millimolar amount, need to be low in order to prevent aggregation of the nanoparticles into large clusters, which significantly limits the amount of material that can be prepared at any one time. Additionally, some of these synthetic pathways also require several additional steps to coat the nanoparticles to prevent aggregation.[12,13]

Presented here is a novel and simple one-step process for creating bulk scale quantities of oxide nanoparticles using, for the first time in these types of syntheses, potassium superoxide (KO_2) to rapidly synthesize nanoparticles from simple salt solutions in water. It is hypothesized that the rapid, exothermic reaction of KO_2 with the salt solutions will rapidly form insoluble oxide or hydroxide nanoparticulates. Because these reactions are performed at very high pH, protection of the nanoparticles formed should not be necessary since the outer coating of the nanoparticles will likely be terminal −OH groups. Additionally, it is likely that the rapid reaction will allow for the use of more concentrated solutions, resulting in multiple grams of nanoparticles from a single, one-step reaction.

2. EXPERIMENTAL SECTION

2.1. Preparation of the Individual Elemental Oxide or Hydroxide Nanoparticles. Starting materials are typically 99.99% purity salts. A variety of starting materials are used including sulfates, chlorides, acetates, and nitrates. Synthesis of the different nanoparticles is performed by adding a 2-fold molar excess of KO_2 to the rapidly stirring salt solution (0.15 M, 100 mL).

Caution! *Care should be taken when working with KO_2 because of its reactive nature. For the second and third row elements, the KO_2 is added quickly; however, for the fifth and sixth row elements, it is observed that the heat generated by the reaction results in the formation of micrometer-sized oxides. Therefore, for these elements, the KO_2 is added slowly over a 10 min time period to prevent the solution from overheating. The reaction is quenched by the addition of 50 mL of methanol shortly after the addition of KO_2 to minimize the particle size. Care should be taken to ensure that all of the KO_2 has reacted prior to the addition of the methanol.*

The resulting suspensions are then centrifuged and repeatedly washed with distilled water until the pH falls to 7. Typically, 5−7

Received: January 31, 2014
Published: April 11, 2014

Figure 1. Illustration of the overall synthetic process: top row, simple salt solutions; middle row, solutions after the addition of KO_2; bottom row, the final nanoparticulate products.

washings are required to bring the pH to 7. The particles are then resuspended and washed twice with methanol. It should be noted that for the blends of nanoparticles, the final methanol rinse is not performed since it is observed that methanol alters the stoichiometry of the blends by removing some of the metals, such as Mn or Co. After the final methanol rinse, the excess methanol is removed and the nanoparticles are vacuum-dried under a dynamic vacuum (10^{-3} Torr) for 12 h, without heating. Typical yields are over 90%.

2.2. Variations of the Standard Preparation. Two variations of the above technique are also explored. For the Mg syntheses, the concentration for the reaction is 0.15 M but is also increased to 1.0 M to determine if there are concentration effects on particle size. These two reactions also use the same, 2-fold molar excess of KO_2 as the other synthetic efforts.

The second variation is to attempt to prepare CuO nanoparticles rather than $Cu(OH)_2$ nanoparticles. It is observed that when the temperature of the solution is increased to 90 °C prior to the addition of KO_2, a mixture of CuO and $Cu(OH)_2$ is formed; however, when the temperature of the solution is increased to 90 °C and a 3-fold molar excess of KO_2 is added, the solution turns black, indicating the presence of CuO, rather than green-blue indicating the presence of $Cu(OH)_2$.

2.3. Synthesis of the Nanoparticulate Blends. Equal molar solutions of LiI and $CoSO_4$ or $Bi(Ac)_3$ and $Mn(Ac)_3$ are used to prepare the Li-ion cathode material, $LiCoO_2$[14] and the multiferroic material, $BiMnO_{3+\delta}$.[15] These solutions are then flash oxidized using KO_2 to prepare nanoparticulate blends of these materials. Because this process allows for the synthesis of gram scale quantities of metal oxide nanoparticles, a third approach to creating nanoparticulate blends is used to prepare the 90 K superconductor, yttrium barium copper oxide (YBCO). For this system, individual reactions are used to prepare grams of nanoparticulate Y_2O_3, BaO_2, and $Cu(OH)_2$. These are then dried and mixed stoichiometrically and suspended in methanol to prepare a precursor nanoink of the oxide nanoparticles. The YBCO precursor is then heated at 940 °C for 8 h and then 425 °C for 12 h, under flowing oxygen.[16]

2.4. Elemental Analysis of the Nanoparticulate Blends. Energy-dispersive analysis of X-rays (EDAX) is performed using a variable pressure Japan Electron Optics Laboratory (JEOL) scanning electron microscope (SEM). Because the reaction with KO_2 is used to prepare oxide nanoparticles primarily using solutions of chlorides, sulfates, or acetates (Ac), EDAX is performed to determine the purity of the metal oxide particulates. Since the anions of the salts studied are sulfate, chloride, and acetate, we studied the composition of Co_3O_4 made from $CoSO_4$, Fe_3O_4 made from $FeCl_2$, and $Ni(OH)_2$ made from $Ni(Ac)_2$.

2.5. X-ray Diffraction Analysis. X-ray diffraction data is collected on a Rigaku SmartLab powder diffraction system equipped with a D/tex 1D detector and a Cu X-ray source. A scan rate of 0.2°/min is used. Post-data-processing uses a Sonneveld−Visser background correction, followed by $k\alpha_2$ stripping. The peak positions are assigned using split pseudo-Voigt peak fitting. The crystal structure and lattice parameter refinement is performed using the PDXL2 Rigaku software package. The overall structural analysis is refined to minimize the %Re and S, where Re is a measure of the residual difference between the calculated and observed diffraction patterns, and where S is the difference between the calculated and observed intensities of the pattern.

2.6. Particle Size Analysis. Several different approaches are used to compare particle sizes: primarily X-ray diffraction (XRD), transmission electron microscopy (TEM), and atomic force microscopy (AFM); although the magnetic data can also be used to support the particle size analysis of the Mn, Fe, Co, and Ni oxide or hydroxide nanoparticles.

2.6.1. XRD Particle Size Analysis. For each oxide nanoparticle prepared, particle size is determined by using the collected X-ray data and the Rigaku PDXL2 program, which calculates particle size using the Halder−Wagner Method.[17] This method accounts for peak broadening effects from both strain and particle size in determining the

Table 1. Summation of Nanoparticle Products and Particle Size Analysis Results[a]

starting material	product	color	Re (%)	S	particle size (nm)	largest unit cell parameter (nm)	ratio of particle size/unit cell
$Y(Ac)_3$-H_2O	Y_2O_3	white	13.75	1.1511	0.12	0.782 (2)	NA
$MgSO_4$	A-$Mg(OH)_2$	white	7.75	1.5225	0.99	0.481 (5)	2
$MgSO_4$	B-$Mg(OH)_2$	white	6.11	1.2387	0.86	0.481 (5)	2
$MgSO_4$	$Mg(OH)_2 \rightarrow$ C-MgO	white	13.92	1.1128	2.49	0.42559 (4)	6
$AlCl_3$-$(H_2O)_x$	AlO-OH	white	9.81	1.0622	3.64	1.24 (4)	3
$Ti(SO_4)_2$	TiO_2 (anatase)	light yellow	5.55	1.4342	0.61	0.903 (11)	NA
$FeCl_2$-$(H_2O)_2$	Fe_3O_4	black	2.00	1.2425	0.53	0.8163 (7)	NA
$Mn(Ac)_3$-$(H_2O)_4$	Mn_3O_4	black	7.5	1.6020	0.54	0.948 (2)	NA
$CoSO_4$	Co_3O_4	black	0.92	1.8092	1.79	0.8023 (4)	2
$Ni(Ac)_2$	$Ni(OH)_2$	light green	2.74	3.7594	1.46	0.461 (3)	3
$Cu(Ac)_2$-$(H_2O)_2$	A-$Cu(OH)_2$	blue-green	5.19	1.4517	2.80	1.0569 (17)	3
$Cu(Ac)_2$-$(H_2O)_2$	B-CuO	black	3.03	1.5466	0.92	0.51256 (5)	2
$Zn(Ac)_2$	A-ZnO_2	white	5.49	1.7804	1.63	0.4865 (3)	3.5
$Zn(Ac)_2$	B-ZnO_2	white	3.67	1.7168	0.42	0.4849 (4)	1
$CeCl_3$	CeO_2	yellow-orange	6.49	1.3617	0.75	0.5664 (11)	1
$SnCl_2$	SnO_2	light yellow	9.10	1.1884	0.85	0.4738 (15)	2
$Tl(Ac)_3$	Tl_2O_3	brown	11.5	1.0592	10.1	1.050175 (6)	10
$PbNO_3$	PbO_2	brown	12.69	1.2209	0.53	0.9727 (12)	NA
LiI + $CoSO_4$	amorphous	black	1.12	1.2615	1.29	1.34 (3)	1
$Bi(Ac)_3$ + $Mn(Ac)_3$	$BiMnO_3$	brown	2.24	2.1343	0.021	0.999	NA
Y_2O_3, BaO_2, and $Cu(OH)_2$	YBCO	brown	6.33	2.1033	NA	NA	NA

[a] NA = not applicable.

average particle sizes for an oxide nanoparticle. In the Supporting Information for each oxide nanoparticle X-ray analysis, a plot of this data is presented for each indexed reflection, where the slope of the line in the Halder−Wagner plot indicates the mean particle size. Previous works have shown that this method of calculating particle size produces comparable results to TEM image analysis, typically within ±5%.[18−22]

2.6.2. TEM Particle Size Analysis. A TEM image is used to confirm the particle size as determined by the XRD analysis. The TEM imaging is obtained using a JEOL 2100 LAB6 TEM. The sample is prepared by suspending the ZnO_2 nanoparticles in methanol, which is dropped onto a copper grid.

2.6.3. AFM Particle Size Analysis. AFM images are collected using an AFM Digital Instruments Dimension 3100. Samples of the nanoparticles are resuspended in methanol and deposited in a thin film onto undoped Si (1 0 0 oriented) wafers that are 0.38 mm thick and are cut into squares (1 cm^2). All scans are collected in tapping mode, typically between 0.2 and 0.25 Hz, and each image is composed of 720 scan lines. A scan of the Si wafer is included in the Supporting Information to demonstrate the surface characteristics of the substrate.

2.7. Thermal Conversion of a Hydroxide Nanoparticle to an Oxide Nanoparticle. Using the high temperature oven feature of the Rigaku SmartLab powder diffraction system, a temperature-dependent study is undertaken to determine at what temperature $Mg(OH)_2$ would convert to MgO, and if the nanoparticulate nature of the material could be maintained. To study the conversion of this hydroxide to an oxide, temperature-dependent studies are performed from 50 to 500 °C, in 50 °C intervals. The sample is annealed for 30 min after each heating step, followed by a 30 min X-ray scan. As such, the sample is annealed for a total of 1 h for each 50 °C interval.

2.8. Magnetic and Electrochemical Analysis. Magnetic measurements are performed on a Quantum Design magnetic property measurement system (MMPS).

Cyclic voltammetry of the $LiCoO_2$ is performed using a VersaSTAT potentiostat in an argon filled glovebox. Two electrode measurements are taken using an ionic liquid electrolyte, 1,2-dimethyl-3-octylimidaziolium bis(trifluoro-methanesulfonyl)imide (MMOI-TFSI), with 1.0 M LiTFSI present and a Li metal anode. Cyclic voltammograms are cycled from 4.5 V down to 3.5 V initially.

The $LiCoO_2$ working electrode is prepared by first grinding a mixture that is 10 wt % graphite (Timcal Timrex KS-6) and 90 wt % nanoparticulates of $LiCoO_2$. The $LiCoO_2$/graphite blend is vacuum-dried for 12 h at 60 °C under a dynamic vacuum (10^{-3} Torr). Small amounts of this mixture are then compressed at 5000 lbs/cm^2 for 10 min onto 0.5 mm × 6 cm gold foil strips (99.9999%). After compression, the gold strips are carefully tapped to ensure that the $LiCoO_2$/graphite mixture is firmly bound to the strip. The gold strips are massed in triplicate before and after the addition of the electrode mixture to allow for accurate capacity calculations. Typically, between 1 and 3 mg of material is deposited.

3. RESULTS AND DISCUSSION

Figure 1 is an example of the broad applicability of this new synthetic pathway because it shows that grams of many different types of nanoparticles can be prepared with one main synthetic step. The first row of Figure 1 shows the initial salt solutions of the different elements. The second row shows the products after the reaction with KO_2 and the addition of methanol. The bottom row shows the grams of nanoparticles after being purified by centrifugation. The complete synthetic results are summarized in Table 1, which lists the starting material, the final type of nanoparticle product, the particle size as calculated by XRD analyses, and the largest unit cell parameter. The low values of %Re and S strongly support the structural X-ray analyses.

It is important to note that certain metals could not be prepared as metal oxide nanoparticulates by this method. Attempts to create nanoparticles using chromium chloride produced water-soluble hydrolyzed metals that did not precipitate out of the solution. Reactions of vanadium sulfate solution with KO_2 did produce particles but in a variety of oxidation states. Solutions of the noble metals salts H_2PtCl_6 and $HAuCl_4$ were also treated with KO_2. Surprisingly, this resulted not in the formation of an oxide, but instead resulted in the formation of nanoparticles of the pure metals: 5 nm Pt particles

Table 2. Unit Cell Data

product	space group	a (Å)	b (Å)	c (Å)	beta	ICDD No.
Y_2O_3	$Ia\bar{3}$	7.82 (2)	7.82 (2)	7.82 (2)	90.0	00-041-1105
A-$Mg(OH)_2$	$Fd\bar{3}m$	3.130 (7)	3.130 (7)	4.81 (5)	90.0, γ = 120.0	01-083-0114
B-$Mg(OH)_2$	$Fd\bar{3}m$	3.20 (5)	3.20 (5)	4.72 (3)	90.0, γ = 120.0	
C-MgO	$Fm\bar{3}m$	4.2559 (4)	4.2559 (4)	4.2559 (4)	90.0	01-071-6452
AlO-OH	*Cmcm*	2.87 (14)	12.4 (4)	3.59 (6)	90.0	01-074-2896
TiO_2 (anatase)	I41/amd	3.806 (17)	3.806 (17)	9.03 (11)	90.0	01-070-8501
Fe_3O_4	$Fd\bar{3}m$	8.163 (7)	8.163 (7)	8.163 (7)	90.0	01-071-6339
Mn_3O_4	I41/amd	5.759 (12)	5.759 (12)	9.48 (2)	90.0	01-071-6262
Co_3O_4	$Fd\bar{3}m$	8.023 (4)	8.023 (4)	8.023 (4)	90.0	03-065-3103
$Ni(OH)_2$	$P\bar{3}m1$	3.105 (7)	3.105 (7)	4.61 (3)	90.0, γ = 120.0	01-074-2075
A-$Cu(OH)_2$	Cmc21	2.954 (3)	10.569 (17)	5.266 (4)	90.0	00-035-0505
B-CuO	C12/c1	4.6854 (5)	3.4307 (3)	5.1256 (5)	99.094 (5)	00-045-0937
A-ZnO_2	$Pa\bar{3}$	4.862 (3)	4.865 (3)	4.865 (3)	90.0	00-013-0311
B-ZnO_2	$Pa\bar{3}$	4.849 (4)	4.849 (4)	4.849 (4)	90.0	
CeO_2	$Fm\bar{3}m$	5.664 (11)	5.664 (11)	5.664 (11)	90.0	01-075-9470
SnO_2	P42/mnm	4.738 (15)	4.738 (15)	3.183 (17)	90.0	01-078-1063
Tl_2O_3	$Ia\bar{3}$	10.50175 (6)	10.50175 (6)	10.50175 (6)	90.0	01-082-0114
PbO_2	*Pbca*	9.727 (12)	5.292 (6)	5.214 (8)	90.0	00-052-0752
$LiCoO_2$	$R\bar{3}m$	2.84 (3)	28.4 (3)	13.4 (3)	90.0, γ = 120.0	01-078-3137
$BiMnO_{3+\delta}$	C1c1, unique-b, cell-1		amorphous, insufficient reflections			01-076-3809
YBCO	*Pmmm*	3.816 (2)	3.885 (6)	11.644 (6)	90.0	01-084-1694

and 2 nm Au particles. Most likely, this is due to the heat generated during the reaction, causing any of the noble metal oxides formed to decompose back into its elemental form. Although LiI is used in the preparation of $LiCoO_2$, because of the nearly insoluble nature of $LiOH\text{-}H_2O$, it is unlikely that this approach will work for the other alkali metals because of their high water solubilities.

As shown in the far right column of Table 1, a comparison between particle size and the largest unit cell parameter indicates that for many of the products listed, the size of the particle is 2−3 times the size of the unit cell. In practical terms, unit cell sized particles would be the lower limit for nanoparticle size, indicating that this technique produces particles with sizes near this lower limit. Table 2 presents the complete unit cell parameters, detailed XRD data, and the International Centre for Diffraction Data (ICDD) (PDF-2/Release 2011 RDB) card number reference for each structural analysis. The Supporting Information also includes the fully indexed diffraction patterns of the different materials and the linear fit used for determining particle sizes based on the fittings of all of the diffraction peaks in each pattern. For several products, the particle size as calculated by the XRD data is less than the largest unit cell parameter, likely indicating that the oxide particle is largely amorphous.

Table 1 lists two different data sets for ZnO_2. A-ZnO_2 refers to the data observed for the ZnO_2 that reacted for 15 min after the addition of the KO_2. B-ZnO_2 is the sample that was prepared by quenching the reaction immediately after the addition of the KO_2 by adding methanol. Figure 2 is used to illustrate two distinct points derived from the XRD patterns. First, the diffraction patterns of A-ZnO_2 and B-ZnO_2, the black and blue lines, respectively, are used to show the significantly broader diffraction peaks when the solution is quenched immediately with methanol. The significantly broader lines of B-ZnO_2 (blue) when compared to A-ZnO_2 (black) provide strong evidence of the reduction in particle size due to quenching of the reaction.

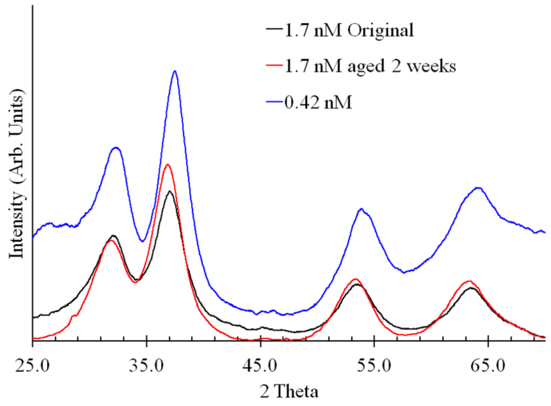

Figure 2. XRD patterns of the different ZnO_2 nanoparticles. The diffraction pattern in black is the original sample immediately after preparation, red is the diffraction pattern of the same sample after aging in air for 2 weeks, and the blue is the smaller particle size ZnO_2 that was generated by immediately quenching the reaction.

The second point illustrated in Figure 2 is that these nanoparticles show significant stability without a protective coating. A-ZnO_2 (black) is the diffraction pattern initially obtained, while A-ZnO_2 (red) is the diffraction pattern observed after the material was stored for 2 weeks. The strong similarity between these two patterns indicates that they are stable for a minimum of 2 weeks, without aggregating to larger particle sizes. This is attributed to the synthesis being performed under very basic conditions, pH ≈ 14.0. As such, the outer oxide coating is likely composed of −OH terminal groups which function to protect the particles from aggregating into larger particles over time. Figure 3 shows the diffraction patterns of several other oxide or hydroxide nanoparticles, illustrating the broad diffraction peaks typically observed for these nanoparticles.

TEM measurements are performed to confirm that the Halder−Wagner analysis of the XRD patterns accurately determines the particle size. Figure 4 shows a high-resolution

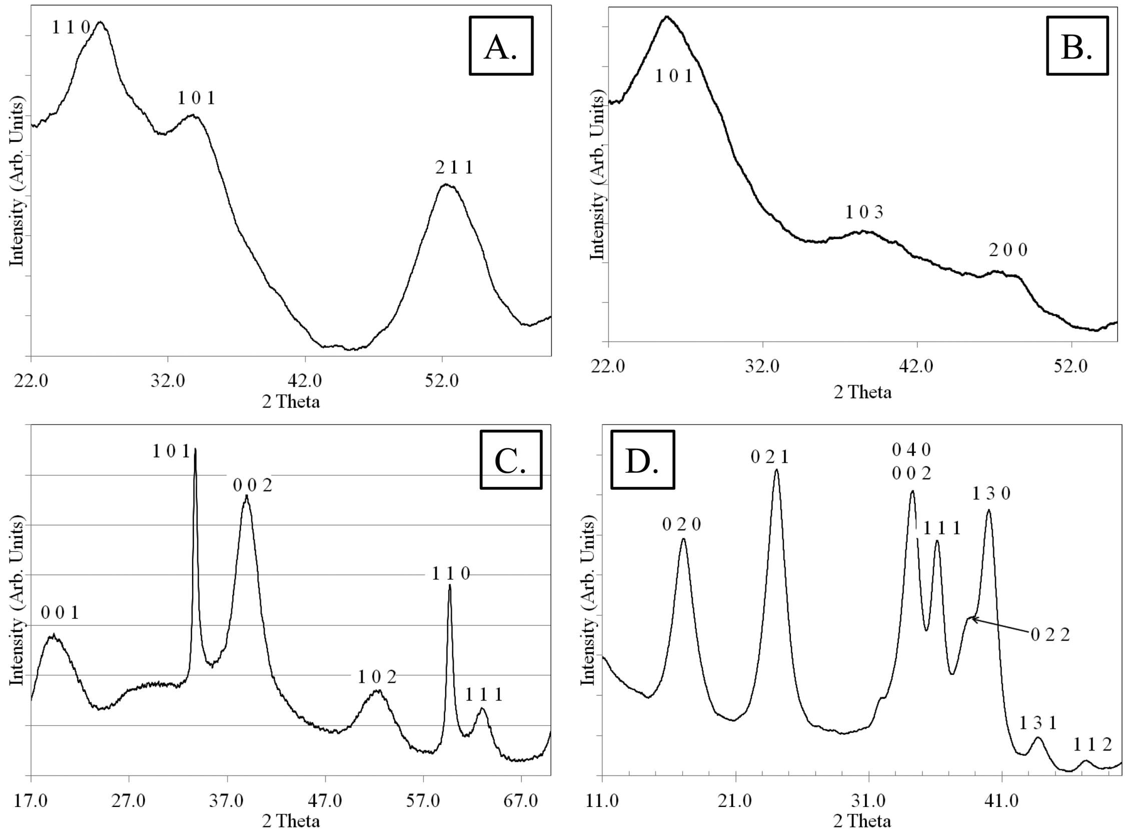

Figure 3. XRD patterns of (A) $Mg(OH)_2$, (B) anatase TiO_2, (C) $Ni(OH)_2$, and (D) $Cu(OH)_2$.

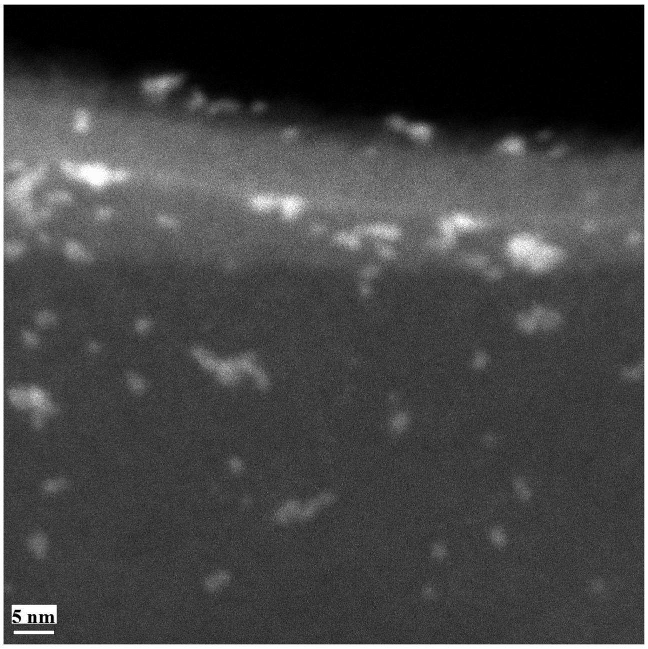

Figure 4. TEM image of the ZnO_2 nanoparticles after aging for 2 weeks.

TEM image of the two week old A-ZnO_2 nanoparticles. As can be seen, TEM analysis indicates an average particle size of 1.7 nm, which as expected, is in very good agreement with the particle size calculated by the X-ray analysis of 1.6 nm.[17−21] The low resolution of the nanoparticles shown in the TEM image likely arises from the poor crystallinity of the samples, which is to be expected due to the rapid rate of this synthetic method.

AFM images are shown for the $Mg(OH)_2$, $Cu(OH)_2$, and CuO in Figure 5, while the AFM images of the Co_3O_4,

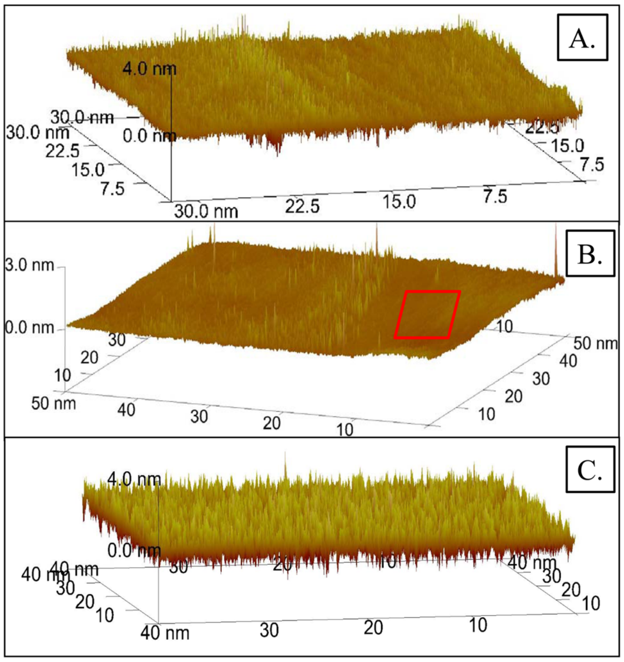

Figure 5. AFM images for (A) $Mg(OH)_2$, (B) $Cu(OH)_2$, and (C) CuO. The red square indicates the smooth surface of the uncoated Si substrate.

$Ni(OH)_2$, and PbO_2 nanoparticles are shown in Figure 6. An AFM image of the uncoated Si substrate (Figure S1) that shows a surface roughness below 20 pm is included in the Supporting Information. The AFM images confirm that for all of these oxide particles, such as the CuO and $Cu(OH)_2$ images, the particle sizes fall within the range that was calculated by the XRD analysis. Perhaps one of the most notable images is that of the PbO_2, Figure 6(C), which indicates particle sizes well below 1.5 nm, as expected. This is in agreement with the cited references which show that careful XRD analysis can yield valid data regarding particles size.

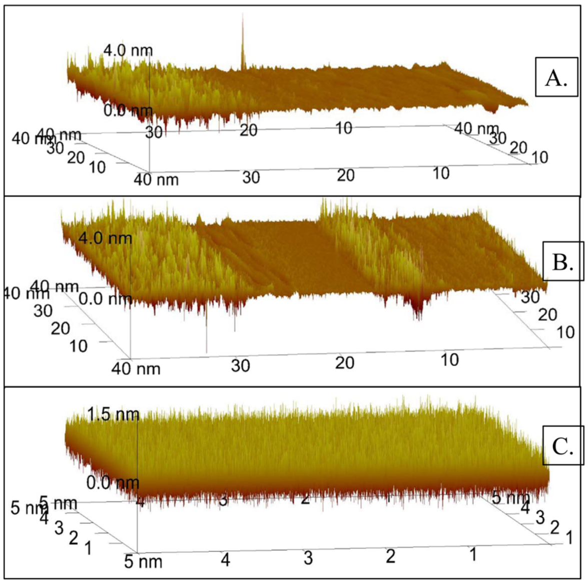

Figure 6. AFM images for (A) $Ni(OH)_2$, (B) Co_3O_4, and (C) PbO_2.

EDAX measurements (Figure 7) indicate only the presence of the metal and oxygen, with no traces of potassium, sulfur, or chlorine, indicating that only a pure metal oxide or hydroxide is formed. This confirms the experimental results that this process is not dependent on the anion to form these oxide nanoparticles, as long as the respective salt is water-soluble.

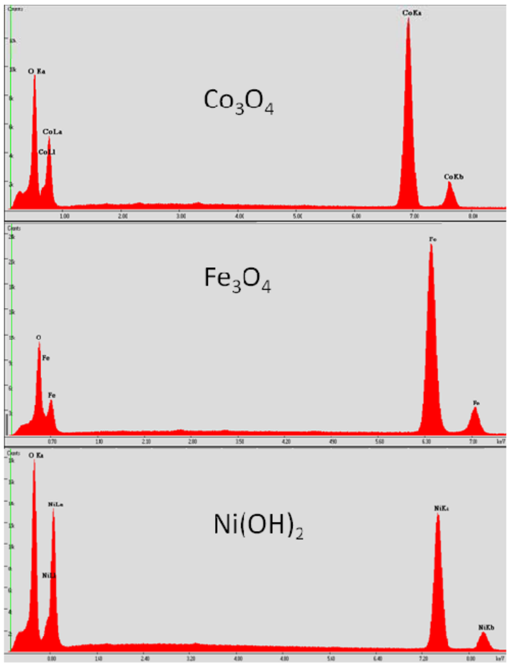

Figure 7. SEM EDAX of the Co, Fe, and Ni oxide particles.

The diffraction patterns obtained at 300, 350, and 400 °C, Figure 8, indicate a transition from magnesium hydroxide to the oxide beginning to occur at 350 °C as expected, and completing when the sample reaches 400 °C. This data is referenced as C-MgO in Table 1 and Table 2. Particle size analysis shows little change as the material undergoes the dehydration reaction; as such, this method of converting the hydroxide nanoparticles into simple oxide nanoparticles could be applicable to other hydroxides.

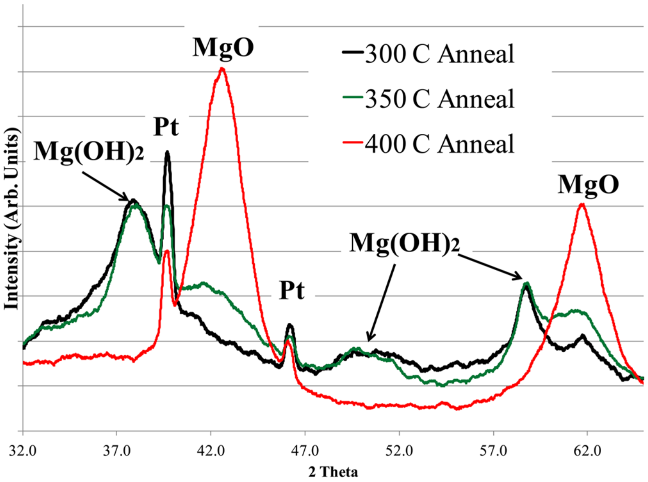

Figure 8. Temperature-dependent XRD patterns at 300, 350, and 400 °C of the conversion of $Mg(OH)_2$ to MgO.

Exploration of the effect of solution temperature on the size and type of nanoparticles formed focuses on the copper acetate solution. Typically, the solution is at room temperature when the 2 mol equiv of KO_2 is added; however, studies indicate that when the copper acetate solution is raised to 90 °C, a mix of CuO and $Cu(OH)_2$ is formed after the addition of a 2-fold molar excess of KO_2. Therefore, by increasing the solution temperature to 90 C, and increasing the amount of KO_2 added to 3 equiv, nanoparticles of pure CuO are formed, These are listed in Table 1 and Table 2 as B-CuO. Visually it is noticeable that as the KO_2 is added, the solution changes from blue to blue-green and then finally to black.

The magnetic behavior of the metal oxide nanoparticulates is studied in part to confirm the structure determinations from the XRD analyses. Figure 9 illustrates the magnetic behavior for several of the different materials. Because of their small size, all of these materials display a variation in their zero field cooled (ZFC) and field cooled (FC) magnetic behavior, and each exhibits a clear ferromagnetic transition at the expected temperature.[23−26] For many magnetic oxide nanoparticles, the strength of the ferromagnetic signal for the FC sample increases relative to the ZFC ferromagnetic signal. In each case shown in Figure 9, the strength of the FC magnetic moment is significantly greater than that of the ZFC sample, which is also indicative of the small particle size of these materials. This provides strong supporting evidence for the structure determination and particle sizes of these metal oxide nanoparticles as determined by the X-ray analysis.

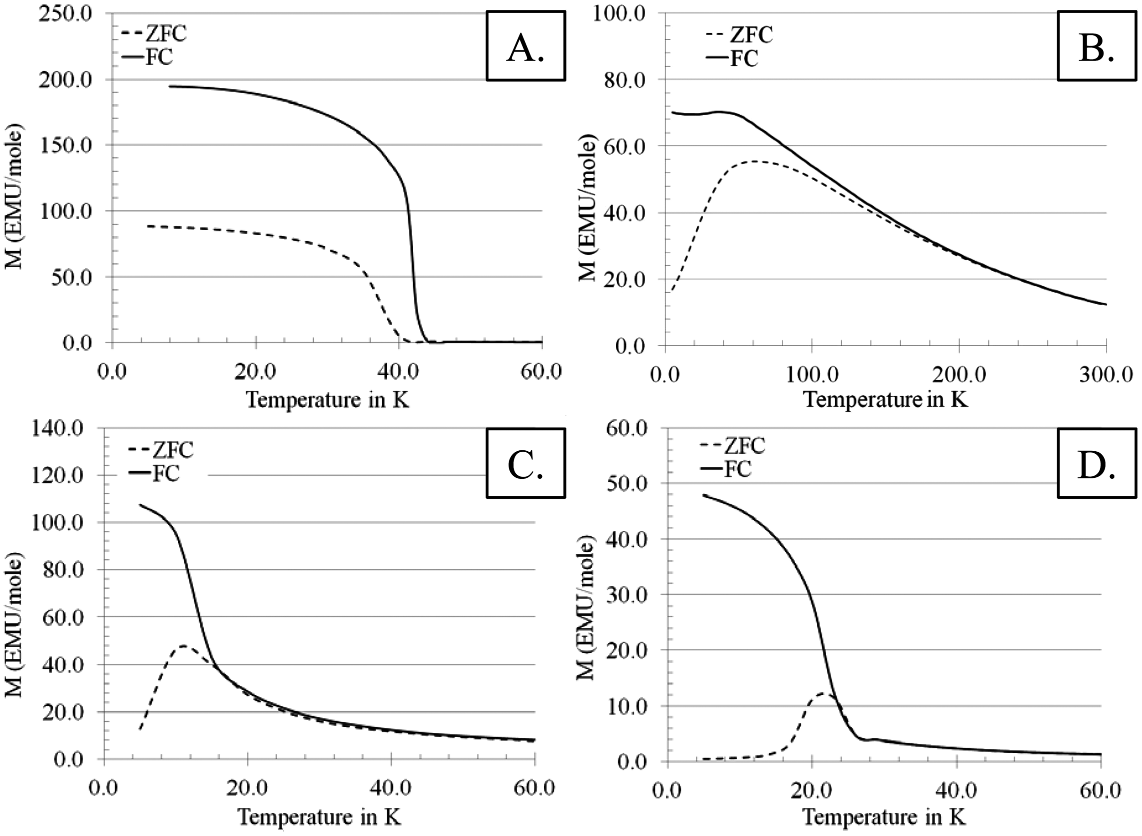

Figure 9. Magnetic behavior of (A) Mn_3O_4, (B) Fe_3O_4, (C) Co_3O_4, and (D). $Ni(OH)_2$.

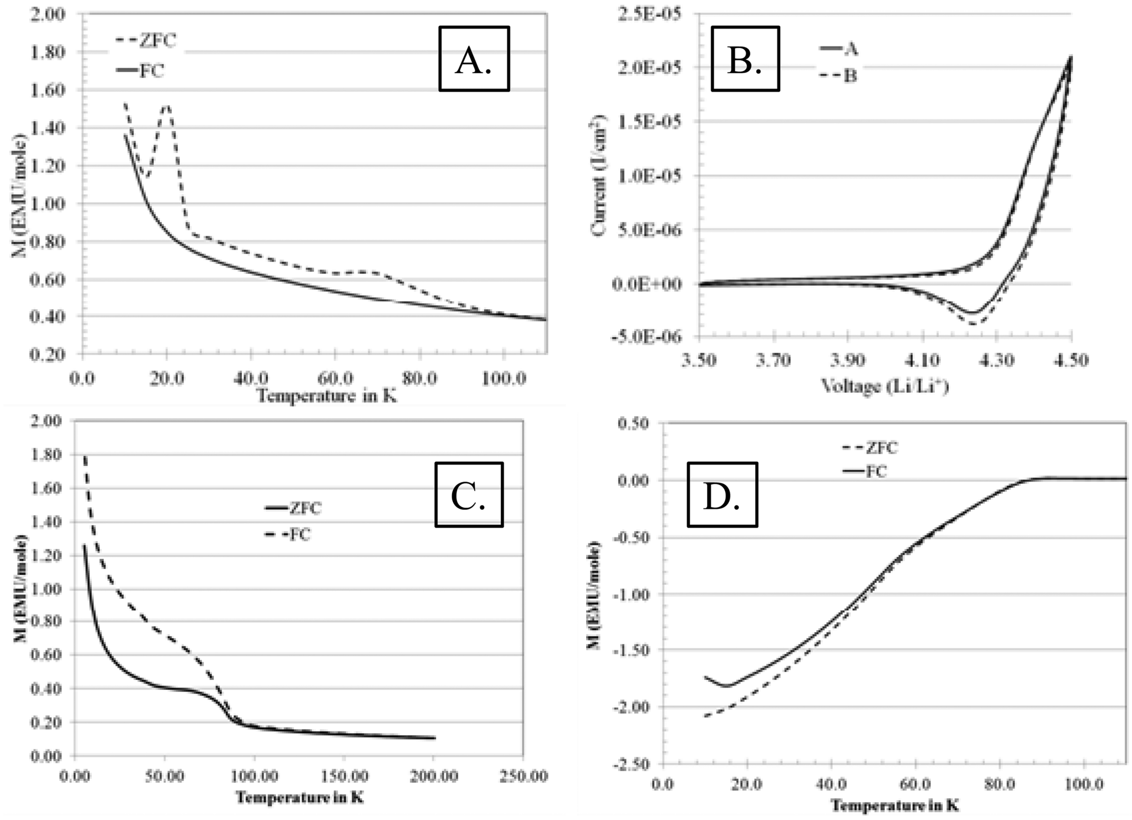

Figure 10. Physical properties of the nanoparticulate blends: (A) magnetic behavior of $LiCoO_2$, (B) first and fifth cyclic voltammogram of $LiCoO_2$ vs Li metal, (C) magnetic behavior of $BiMnO_{3+\delta}$, and (D) superconducting transition of the 90 K superconductor YBCO.

One interesting aspect of this work is the preferential formation of the M_3O_4 phase for the Mn, Fe, and Co nanoparticles, which was confirmed by their magnetic behavior. For iron and cobalt the starting material was +2, and as expected, the final product was oxidized to an average of +2.33. However, in the case of Mn, the starting material was +3 but in the final product, the Mn was reduced to +2.33. As such, it seems that from a room temperature solution and with this stoichiometry of a 2-fold excess of KO_2, the M_3O_4 structure is preferred, even if reduction is required to form this phase.

Results of the two alternative approaches are also of significant interest. As shown in Table 1 and Table 2, the $Mg(OH)_2$ nanoparticles are prepared at two different concentration strengths. The A-$Mg(OH)_2$ is prepared at a concentration of 0.15 M, as is done for all other samples. The B-$Mg(OH)_2$, however, is prepared from a 1 M solution of $MgSO_4$. Even at this high concentration, which allowed for the preparation of over 10 g of oxide nanoparticles in a single synthesis, the XRD assessment indicates that these nanoparticles are all near 1 nm in size.

To test this approach in the synthesis of blends of oxide nanoparticulates, several additional materials are prepared. X-ray analysis of the prepared $LiCoO_2$ and $BiMnO_{3+\delta}$ blend shows that the initial product from these reactions is highly amorphous. Therefore, these two systems are heat treated by being annealed under flowing oxygen at 150 and 200 °C, respectively, for 6 h. The annealed $LiCoO_2$ then displays the expected diffraction pattern (Supporting Information) and magnetic behavior, Figure 10A. The $LiCoO_2$ is also characterized via cyclic voltammetry, Figure 10B. Deintercalation and intercalation of Li^+ occurs at the expected voltages for this cathode material, while the similarity between the first and fifth cycles provides strong evidence that the correct stoichiometry is $LiCoO_2$.[14] Although the XRD of $BiMnO_{3+\delta}$ only indicates two very broad peaks, it still exhibits the expected ferromagnetic transition, Figure 10C, at near 90 K. This low transition temperature is also indicative of the high oxygen content of the annealed sample, with δ equal to 0.1 or greater.[15]

The 90 K superconducting transition of the YBCO, Figure 10D, and the similar behavior between the ZFC and FC samples strongly suggests a high purity phase, as is observed in the XRD pattern provided in the Supporting Information, Figure S2.[16] This provides strong evidence that this is a viable alternative path for preparing the YBCO superconductor. Previous methods for preparing the YBCO superconductor involved the use of trifluoroacetates. These solutions were used to coat surfaces which were then heated to prepare the YBCO superconductors. However, the presence of the trifluoroacetate requires a complicated heating scheme under several different atmospheres in order to ensure that the proper YBCO phase is formed.[27] Since this method uses a suspension of oxide nanoparticles rather than a trifluoroacetate solution, the correct YBCO phase can be obtained using a simplified heating process as is detailed in the methods section. As such, this approach is likely amenable to prepare thin films of higher critical transition temperature (T_c) materials, such as the Bi, Tl, or Hg superconductors. This work also provides a new alternative path toward developing oriented or partially oriented thin films from solutions of oxide nanoparticles for superconductors as well as many multiferroic or solar cell materials.

4. CONCLUSION

The work presented here provides a promising new path for preparing bulk quantities of many different types of oxide nanoparticles or blends of oxide nanoparticles. These results also point to many other possibilities. The preference for certain elements to form the M_3O_4 phase, even if reduction of the metal is required, is one notable result. The formation of noble metal nanoparticles instead of oxides is also an interesting new path for the formation of nanoparticulate noble metals. Finally, the change in reaction conditions used to generate CuO rather than $Cu(OH)_2$ may indicate that altering the reaction conditions or the amount of KO_2 added could result in the formation of other types of oxide nanoparticles, such as pure Al_2O_3 or Fe_2O_3.

The results and analyses show that not only can multiple elements be converted to oxide nanoparticles by this method, but also the results for the $LiCoO_2$, $BiMnO_{3+\delta}$, and YBCO syntheses indicate that this process can be used to prepare many novel materials. As such, this new synthetic route to oxide nanoparticles also shows great promise for a multitude of other catalytic, electrical, magnetic, or electrochemical systems, from novel cathodes to other types of ceramic materials.

■ ASSOCIATED CONTENT

Ⓢ Supporting Information

Supporting AFM and complete data set of all XRD data. This material is available free of charge via the Internet at http://pubs.acs.org.

■ AUTHOR INFORMATION

Corresponding Author

*E-mail: thomas.sutto@nrl.navy.mil.

Funding

This work was funded by the Office of Naval Research (ONR) through the Naval Research Laboratory Basic Research Program.

Notes

The authors declare no competing financial interest.

■ ACKNOWLEDGMENTS

The author would like to gratefully acknowledge Nabil Bassim for the TEM imaging.

■ REFERENCES

(1) Ekimov, A. I.; Efros, A. L.; Onushchenko, A. A. *Solid State Commun.* **1985**, *56*, 921−924.

(2) Zhao, X. Q.; Liang, Y.; Cui, Z. J.; Xiao, K.; Zheng, F.; Hu, Z. Q. *Nanostruct. Mater.* **1994**, *4*, 397−404.

(3) Neouze, M.-A. *J. Mater. Sci.* **2013**, *48*, 7321−7349.

(4) Arico, A. S.; Bruce, P.; Scrosati, B.; Tarascon, J.-M.; Schalkwijk, W.V. *Nat. Mater.* **2005**, *4*, 366−377.

(5) Luo, X.; Morrin, A.; Killard, A. J.; Smith, M. R. *Electroanalysis* **2006**, *18*, 319−326.

(6) Chen, H. M. *Mater. Sci. Eng., R* **2013**, *74*, 35−69.

(7) O'Regan, B.; Grätzel, M. *Nature* **1991**, *353*, 737−740.

(8) Panero, S.; Scrosatia, B.; Wachtlera, M.; Croceb, F. *J. Power Sources* **2004**, *129*, 90−95.

(9) Brock, S. L.; Sanabria, M.; Nair, J.; Suib, S. L.; Ressler, T. *J. Phys. Chem. B* **2001**, *105*, 5404−5410.

(10) Wang, P.; Zakeeruddin, S. M.; Comte, P.; Exnar, I.; Grätzel, M. *J. Am. Chem. Soc.* **2003**, *125*, 1166−1167.

(11) Ha, D.-H.; Islam, M. A.; Robinson, R. D. *Nano Lett.* **2012**, *12*, 5122.

(12) Khadzhiev, S. N.; Kadiev, K. M.; Yampolskaya, G. P.; Kadieva, M. K. *Adv. Colloid Interface Sci.* **2013**, *197*, 128−132.
(13) Niederberger, M.; Garnweitner, G. *Chem.—Eur. J.* **2006**, *12*, 7282−7302.
(14) Artemenko, A.; Ménétrier, M.; Pollet, M.; Delmas, C. *J. Appl. Phys.* **2009**, *106*, 0649141.
(15) Belik, A. A.; Kodama, K.; Igawa, N.; Shamoto, S.; Kosuda, K.; Takayama-Muromachi, E. *J. Am. Chem. Soc.* **2010**, *132*, 8137−8144.
(16) Wu, M. K.; Ashburn, J. R.; Torng, C. J.; Hor, P. H.; Meng, R. L.; Gao, L.; Huang, Z. J.; Wang, Y. Q.; Chu, C. W. *Phys. Rev. Lett.* **1987**, *58*, 908−910.
(17) Halder, N. C.; Wagner, C. N. J. *Acta Crystallogr.* **1966**, *20*, 312−313.
(18) Borchert, H.; Shevchenko, E. V.; Robert, A.; Mekis, I.; Kornowski, A.; Grübel, G.; Weller, H. *Langmuir* **2005**, *21*, 1931−1936.
(19) Mubarak, T. H.; Hassan, K. H.; Abbas, Z. M. A. *Adv. Mater. Res.* **2013**, *685*, 119−123.
(20) Lock, N.; Jensen, E. M. L.; Mi, J.; Mamakhel, A.; Norén, K.; Qingboc, M.; Iversen, B. B. *Dalton Trans.* **2013**, *42*, 9555−9564.
(21) Popescu, R.; Leidinger, P.; Kind, C.; Feldmann, C.; Gerthsen, D. *J. Nanopart. Res.* **2013**, *15*, 1648−1664.
(22) Chaki, S. H.; Sunil, H.; Deshpande, M. P.; Chaudhary, M. D.; Mahesh, D.; Mahato, K. S.; Kanchan, S. *Adv. Sci., Eng. Med.* **2013**, *5*, 285−290.
(23) Gopalakrishnan, K.; Bagkar, N.; Ganguly, R.; Kulshreshtha, S. K. *J. Cryst. Growth* **2005**, *280*, 436−441.
(24) Parvin, K.; Ma, J.; Ly, J.; Sun, X. C.; Nikles, D. E.; Sun, K.; Wang, L. M. *J. Appl. Phys.* **2005**, *95*, 7121−7123.
(25) Ichiyanagi, Y.; Yamada, S. *Polyhedron* **2005**, *24*, 2813−2816.
(26) Rall, D.; Seehra, M. S. *J. Phys.: Condens. Matter* **2012**, *24*, 7602−7610.
(27) Yan, G.; Liu, C. F.; Feng, Y.; Zhang, P. X.; Wu, X. Z.; Zhou, L. *Physica C* **2003**, *396*, 913−922.

■ NOTE ADDED AFTER ASAP PUBLICATION

This paper was published on the Web on April 11, 2014, with errors in Figure 9. The corrected version was reposted on May 5, 2014.